

Article

A Study on the Energy Absorption Performance of Mine Grooved Conical Tube Energy Absorption Components

Ziyang Li ¹, Xiaochun Xiao ^{1,*}, Jun Xu ¹ and Bin Sun ^{2,*}

¹ School of Mechanics and Engineering, Liaoning Technical University, Fuxin 123000, China; liuqi@lntu.edu.cn (Z.L.); xujun@lntu.edu.cn (J.X.)

² Department of Engineering Mechanics, Southeast University, Nanjing 211189, China

* Correspondence: xiaoxiaochun@lntu.edu.cn (X.X.); binsun@seu.edu.cn (B.S.)

Abstract: When rockbursts occur, hydraulic support is prone to impact failure, which leads to severe casualties and economic losses. To improve the performance of hydraulic support structures under impact loading, a grooved conical tube is designed as an energy absorption device to avoid hydraulic columns being destroyed. The performance of the grooved conical tube during deformation is studied using simulation, considering the wall thickness, cone angle and number of grooves. The equivalent axial load of the grooved conical tube component is derived by studying the energy dissipation path. And the grooved conical tube's structure is optimized. The results show that the Y3-5-10 (cone angle: 3°; number of grooves: 5; wall thickness: 10 mm) grooved conical tube shows excellent performance among the twenty-seven types of structures. In addition, the equivalent axial load prediction formula for the grooved conical tube has a high prediction accuracy. Furthermore, after multi-objective optimization, the mean square error is decreased by 20.6%, and the effective energy absorption is increased by 6.0%, which is able to make the energy absorption process more stable. Compared with widely used corrugated square tubes, the effective deformation distance of the grooved conical tube is increased by 27.2%, and the effective energy absorption is increased by 37.1%. The grooved conical tube has advantages in its effective deformation distance and effective energy absorption. These results are expected to provide sufficient time for the opening of the support column's relief valve and to enhance the impact resistance of the hydraulic support, which is highly important for the prevention of rockbursts.



Academic Editor: Eugeniusz Koda

Received: 29 December 2024

Revised: 26 January 2025

Accepted: 28 January 2025

Published: 30 January 2025

Citation: Li, Z.; Xiao, X.; Xu, J.; Sun, B. A Study on the Energy Absorption Performance of Mine Grooved Conical Tube Energy Absorption Components. *Buildings* **2025**, *15*, 437. <https://doi.org/10.3390/buildings15030437>

Copyright: © 2025 by the authors. Licensee MDPI, Basel, Switzerland. This article is an open access article distributed under the terms and conditions of the Creative Commons Attribution (CC BY) license (<https://creativecommons.org/licenses/by/4.0/>).

Keywords: grooved conical tube; rockburst; hydraulic support; multi-objective optimization; energy absorption performance

1. Introduction

With the exhaustion of shallow coal resources and the development of coal mining to greater depths, a drastic mining response is inevitable. The frequency of roadway rockbursts has increased significantly, resulting in severe casualties and economic losses [1–3]. Hydraulic support is the main supporting equipment in coal mine roadways. When rockbursts occur, the relief valve of the hydraulic column cannot be opened in time, leading to the destruction of the hydraulic column or even a cylinder explosion, as shown in Figure 1 [4–6].

Pan et al. [7,8] proposed anti-impact support theory based on traditional hydraulic support. The component is connected to the hydraulic column to absorb the impact energy, which provides sufficient time for the opening of the relief valve and prevents the failure of the support system. Considerable valuable research has been conducted

on the components of anti-impact support. Ma et al. [9,10] designed a corrugated square tube component based on the progressive folding deformation of thin-walled square tubes. The buckling deformation mode of the component was guided by the pre-fold surface, and the performance of the component was tested under cyclic loading and unloading. However, the process of the pre-folded component is complicated, and the pre-folded structure decreases the deformation distance of the corrugated square tube. Tian et al. [11,12] designed a multi-cell circular tube energy absorption component based on simplified super-folded element theory. The multi-cell circular tube was divided into different shapes and numbers of basic deformation units, and the equivalent axial load prediction formula for a multi-cell circular tube with different section shapes under an axial impact was analyzed. The influence of the structural parameters on the performance of the multi-cell circular tube was investigated numerically. However, the component exhibits poor stability during deformation. Hao et al. [13] designed a buffering device combining a rigid structure and filling material. The buffer device can be recycled and can be easily removed and replaced when the filling material has consumed the external impact energy. The performance of buffer devices with different filling materials was verified using experiments, but the structure of the buffer device is complicated. Yang et al. [14] designed an expanded component. In the process of axial collapse, the expanded component has a repeatable deformation and failure mode, and the component expands to the outer ring after the expanding deformation. However, the buckling length and energy absorption of the expanded component are limited, resulting in a narrow application range. Guo et al. [15] proposed a threaded shear component and designed the thread profiles of triangle, rectangle and ladder, respectively. Through a parametric analysis of the screw diameter and thread pitch of the component, the influence of the screw diameter and thread pitch on its energy absorption performance was investigated. However, the component cannot fully utilize the base space of the hydraulic column. Wang et al. [16] designed a rib-plate tube which inhibits Euler instability during the collapse by using the rib-plate to increase the boundary constraint. Compared with thin-walled circular tubes, the deformation mode of rib-plate circular tubes transforms into a mixed deformation mode. However, the rib-plate circular tube is prone to cracking during buckling deformation, and this effect is not optimal for its practical application. Zhang et al. [17] designed a twisted plate component using simulation and investigated the impacts of rounded corners, the wall thickness and the number and radius of the ripples on its performance. The component has a controllable deformation mode, but the structure of the component is complex, and its effective deformation distance is short. According to the above investigations, thin-walled metal tubes are widely used in supports. However, the performance of the existing components still has excellent potential for improvement, especially in terms of an effective deformation distance and effective energy absorption.

This study takes the ZHD6000-type support (Beijing Chengtian Hengye Coal Mine Equipment Co., Ltd., Beijing, China) [18] as the application system and proposes a grooved conical tube energy absorption component. The component produces a steady accordion buckling mode [19]. Firstly, the energy dissipation path of the grooved conical tube components is analyzed, and an equivalent axial load prediction formula for the grooved conical tube components is derived. In addition, the performance of grooved conical tube components of different structural types was analyzed through simulations of the axial impact. The structure with the best performance among the different structural types of grooved conical tubes was selected, and the accuracy of the equivalent axial load prediction formula was verified. Finally, with the aim of minimizing the mean square error and maximizing the effective energy absorption, a multi-objective optimization model was established to investigate the effect of the groove width and the groove depth on the

performance of the grooved conical tube. It provides a new structural component for hydraulic support columns and improves the effective deformation distance and effective energy absorption compared to those of the existing corrugated square tubes which are widely used. The grooved conical tube provides sufficient time to open the relief valve of the hydraulic support column, which is crucial for the prevention of rockbursts.



Figure 1. Impact destruction of hydraulic supports. (a) Support failure. (b) Column bend. (c) Cylinder burst. (d) Beam failure.

2. Structural Design Options and Evaluation Indicators

2.1. Structural Design of the Grooved Conical Tube

The structure of a grooved conical tube component is designed and applied to the ZHD6000 energy absorption anti-impact support. The installation position of the grooved conical tube component is shown in Figure 2.

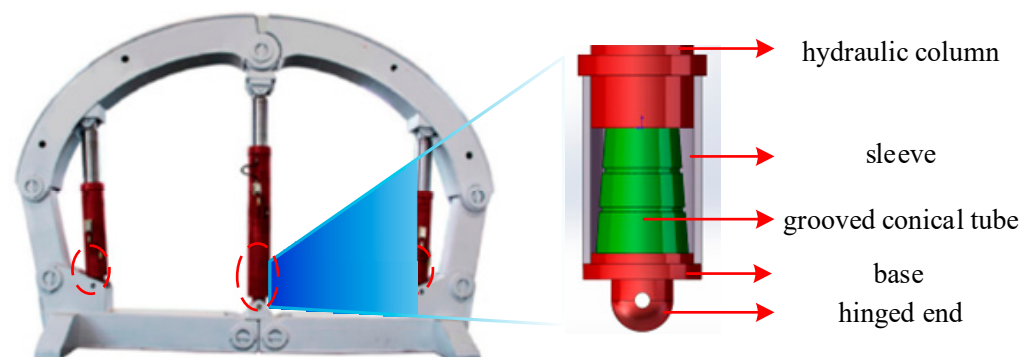


Figure 2. Mounting position of the grooved conical tube.

Figure 3 shows the grooved conical tube component with five grooves. The height (H) of the grooved conical tube is 360 mm, and its bottom radius (R) is 180 mm. In Figure 3, φ represents the cone angle, d is the groove depth, w is the groove width, λ represents the

distance between the midpoints of two grooves, b is the number of grooves and t is the wall thickness of the grooved conical tube. The groove depth is half the thickness, and the width is equal to the thickness. Its special shape and grooves are used to guide the component to deform rapidly under impact, and the performance of the conical tube is improved.

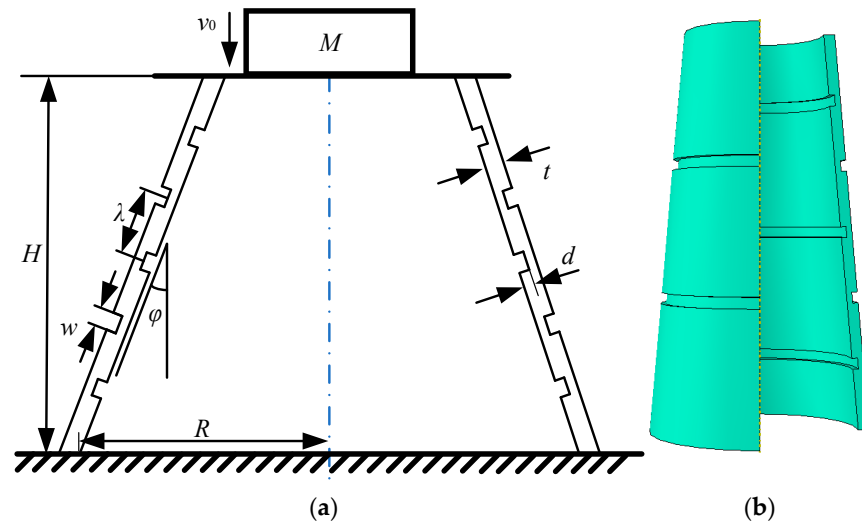


Figure 3. Structures of grooved conical tube component. (a) Two-dimensional. (b) Three-dimensional.

The ranges of cone angles, groove numbers and wall thicknesses suitable for the grooved conical tube of the ZHD6000 anti-impact support were determined using simulation in advance. Grooved conical tubes with different cone angles, groove numbers and wall thicknesses were designed to study the performance of components with different structural types under an impact load. The design scheme for the grooved conical tube component is shown in Table 1. The grooved conical tube components for each structural type were named using the following convention: “cone angle-groove number-wall thickness”. For example, Y3-5-10 represents a grooved conical tube with a cone angle of 3°, 5 grooves and a wall thickness of 10 mm.

Table 1. Structural design scheme of grooved conical tube component.

Specimen Type	H/mm	R/mm	$\varphi/^\circ$	$b/Number$	t/mm
Y3-5-10	360	180	3	5	10
Y3-5-12	360	180	3	5	12
Y3-5-14	360	180	3	5	14
Y3-7-10	360	180	3	7	10
Y3-7-12	360	180	3	7	12
Y3-7-14	360	180	3	7	14
Y3-9-10	360	180	3	9	10
Y3-9-12	360	180	3	9	12
Y3-9-14	360	180	3	9	14
Y5-5-10	360	180	5	5	10
Y5-5-12	360	180	5	5	12
Y5-5-14	360	180	5	5	14
Y5-7-10	360	180	5	7	10
Y5-7-12	360	180	5	7	12
Y5-7-14	360	180	5	7	14
Y5-9-10	360	180	5	9	10
Y5-9-12	360	180	5	9	12
Y5-9-14	360	180	5	9	14

Table 1. Cont.

Specimen Type	H/mm	R/mm	$\varphi/^\circ$	b/Number	t/mm
Y7-5-10	360	180	7	5	10
Y7-5-12	360	180	7	5	12
Y7-5-14	360	180	7	5	14
Y7-7-10	360	180	7	7	10
Y7-7-12	360	180	7	7	12
Y7-7-14	360	180	7	7	14
Y7-9-10	360	180	7	9	10
Y7-9-12	360	180	7	9	12
Y7-9-14	360	180	7	9	14

2.2. Evaluation Indicators of the Grooved Conical Tube

In the design process for the support, the component is connected to the column to bear the load during the working process. When the load of the support exceeds the rated resistance, the component directly deforms as a buffer structure, and the energy of the impact load is transformed into deformation energy, providing adequate time for the relief valve of the column to be opened. The performance of the component is evaluated using the following evaluation indicators:

- (1) The initial peak load [11], P_{\max} ,

$$F_1 < P_{\max} < 1.5F_1 \quad (1)$$

where F_1 is the rated resistance of the support;

- (2) The effective deformation distance [12], δ_{ef} , is the buckling length of the grooved conical tube when the load reaches the P_{\max} for the second time in the process of axial crushing;
- (3) The effective energy absorption [13], E_{tot} , represents the energy absorption when the load reaches the P_{\max} for the second time in the process of axial crushing:

$$E_{tot} = \int_0^s F(x)dx \quad (2)$$

where s is the buckling length of the grooved conical tube, and $F(x)$ is the load when the buckling length reaches x ;

- (4) The mean load [14], P_{mean} , reflects the bearing capacity of the grooved conical tube in the process of axial crushing:

$$P_{\text{mean}} = \frac{E_{\text{tot}}}{\delta_{\text{ef}}} \quad (3)$$

- (5) The mean square error [15], σ , reflects the fluctuation in the load in the process of axial crushing:

$$\sigma = \sqrt{\frac{1}{n}[F(x) - P_{\text{mean}}]^2} \quad (4)$$

where n is the total number of data points.

Based on the design requirements for the components of a support, the initial peak load should be as large as possible within the standard range of the components; the effective deformation distance and the effective absorption energy should be as large as possible; and when the mean square error is small, the mean load should be as close as possible to the initial peak load, which will make the energy absorption process more stable.

3. A Theoretical Model of the Equivalent Axial Load

In this study, based on a theoretical model of the impact of thin-walled circular tubes [20], the energy dissipation path of the grooved conical tube components was analyzed. A theoretical model of the energy absorption of the grooved conical tube components under an axial impact was established, as shown in Figure 4. It was presumed that the material was ideally rigid–plastic and that bending and stretching would not interact in the yield criterion [21].

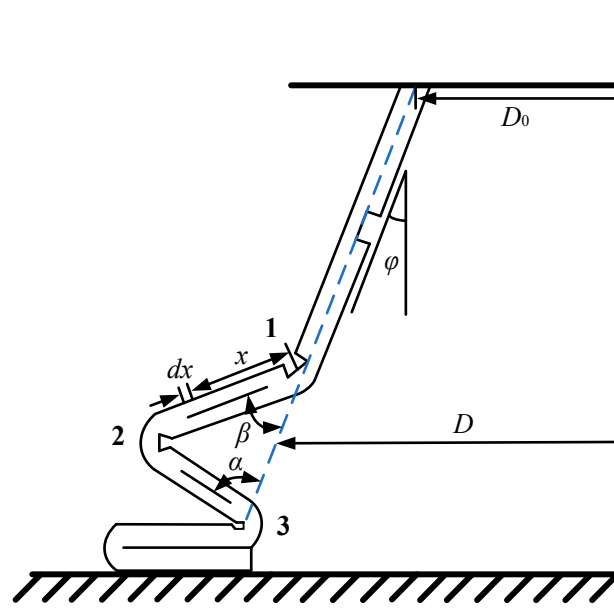


Figure 4. Deformation diagram of grooved conical tube component.

The energy dissipated under the axisymmetric folding deformation mode of the grooved conical tube mainly includes two parts: (1) the energy dissipated by the formation of bending plastic hinges, E_b , and (2) the energy dissipated by the tensile deformation of the materials between the plastic hinges, E_s . When a fold is completely flattened in the deformation process of the component, three plastic hinges appear, and the energy dissipated through plastic bending at plastic hinges 1, 2 and 3 is as follows:

$$E_b^1 = M_p \int_0^{\frac{\pi}{2} - \varphi} \pi [D - 2\lambda \cos(\beta + \varphi) \tan \varphi] d\beta \quad (5)$$

$$E_b^2 = M_p \int_0^{\frac{\pi}{2} + \varphi} \pi [D + 2\lambda \sin(\alpha - \varphi) + 2\lambda \cos(\alpha - \varphi) \tan \varphi] d\alpha \quad (6)$$

$$+ M_p \int_0^{\frac{\pi}{2} - \varphi} \pi [D + 2\lambda \sin(\beta + \varphi) - 2\lambda \cos(\beta + \varphi) \tan \varphi] d\alpha$$

$$E_b^3 = M_p \int_0^{\frac{\pi}{2} + \varphi} \pi [D + 2\lambda \cos(\alpha - \varphi) \tan \varphi] d\alpha \quad (7)$$

where λ is the distance between the midpoints in the two grooves, φ is the cone angle and M_p is the plastic limit bending moment per unit width.

$$M_p = \frac{2}{\sqrt{3}} \sigma_0 \frac{(t')^2}{4} \quad (8)$$

where σ_0 is the yield stress, and t' is the wall thickness of the groove.

The energy dissipated through stretching is:

$$E_s = 2 \left\{ \int_0^{\frac{w}{2}} \pi(D_0 + 2x \sin \varphi) t' \sigma_0 \ln \left[\frac{2x \sin(\alpha - \varphi) + 2x \cos(\alpha - \varphi) \tan \varphi + D_0 + 2x \sin \varphi}{D_0 + 2x \sin \varphi} \right] dx \right. \\ + \int_{\frac{w}{2}}^{\lambda - \frac{w}{2}} \pi(D_0 + 2x \sin \varphi) t \sigma_0 \ln \left[\frac{2x \sin(\alpha - \varphi) + 2x \cos(\alpha - \varphi) \tan \varphi + D_0 + 2x \sin \varphi}{D_0 + 2x \sin \varphi} \right] dx \\ \left. + \int_{\frac{w}{2}}^{\frac{\lambda}{2}} \pi(D_0 + 2x \sin \varphi) t' \sigma_0 \ln \left[\frac{2x \sin(\alpha - \varphi) + 2x \cos(\alpha - \varphi) \tan \varphi + D_0 + 2x \sin \varphi}{D_0 + 2x \sin \varphi} \right] dx \right\} \quad (9)$$

where w is the width of the groove, when $\alpha = \frac{\pi}{2} + \varphi$.

$$\ln \left[\frac{2x \sin(\alpha - \varphi) + 2x \cos(\alpha - \varphi) \tan \varphi + D_0 + 2x \sin \varphi}{D_0 + 2x \sin \varphi} \right] \approx \frac{2x}{D_0 + 2x \sin \varphi} = \frac{2x}{D} \quad (10)$$

Substituting the result of Equation (10) into Equation (9), the energy dissipated by stretching can be obtained as follows:

$$E_s = 2\pi\sigma_0 (\lambda^2 t - \lambda w t + \lambda w t') = 2\pi\sigma_0 \lambda (\lambda t - w d) \quad (11)$$

where d is the groove depth, and t is the wall thickness of the grooved conical tube.

According to the conservation of energy, the work done by the external load on the grooved conical tube is equal to the sum of the energy dissipated by the plastic bending and stretching of the component:

$$\sum_{i=1}^k (E_b^1 + E_b^2 + E_b^3 + E_s) = \overline{P}_m \times \delta_{ef} \quad (12)$$

where \overline{P}_m is the equivalent axial load, δ_{ef} is the effective deformation distance and k is the number of grooves in the inner wall of the grooved conical tube. According to the coefficient of effective deformation distance [22]:

$$\delta_{ef} = 0.87H \left(1 - \frac{t}{\lambda} \right) \quad (13)$$

where H is the height of the grooved conical tube, the equivalent axial load of the grooved conical tube is:

$$\overline{P}_m = \frac{\sum_{i=1}^k (E_b^1 + E_b^2 + E_b^3 + E_s)}{0.87H \left(1 - \frac{t}{\lambda} \right)} \quad (14)$$

The equivalent axial load of the Y3-5-10 grooved conical tube is:

$$\overline{P}_m = \frac{\sum_{i=1}^3 \left(\frac{\pi\sigma_0(t')^2}{\sqrt{3}} (\pi D_i + 2.01\lambda) + 2\pi\sigma_0 \lambda (\lambda t - w d) \right)}{0.87 \times 360 \left(1 - \frac{t}{\lambda} \right)} \quad (15)$$

4. The Performance of the Grooved Conical Tubes

4.1. The Grooved Conical Tube Simulation Model

According to the structure of the component in the support column, the component of the hydraulic column mainly bears the axial impact load at the top, and the bottom is fixed during the working process [23]. The base and column are simplified as rigid plates, and the impact load is applied to the upper rigid plate to simulate the impact load of the column. As shown in Figure 5, the finite element software ABAQUS (2020) was used to establish an axial impact model for the grooved conical tube energy absorption component, and the display dynamic analysis module was used to complete the simulation of the impact of the grooved conical tube energy absorption component.

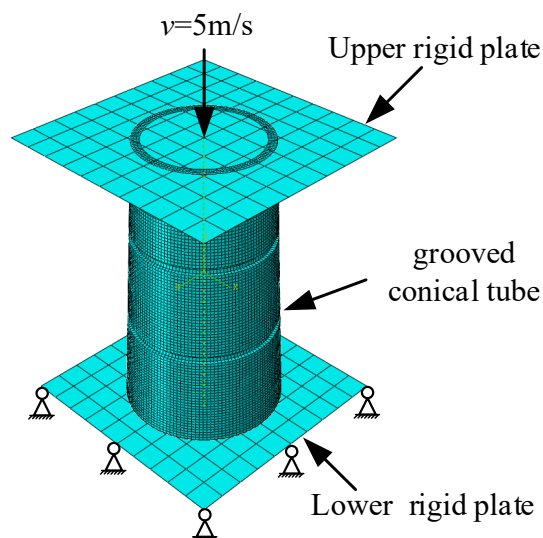


Figure 5. Simulation model.

The lower surface of the grooved conical tube component is connected to the lower rigid plate and restricts the degrees of freedom in all directions, while the upper rigid plate restricts the degrees of freedom in all directions except the axial direction for the grooved conical tube. General contact is adopted for the grooved conical tube components. The coefficient of friction in the tangential direction is set to 0.25, and normal contact is set to hard contact [16]. Based on data on rockbursts [24], the impact load of the upper rigid plate is set to 5 m/s. The grooved conical tube experiences large plastic deformation after the impact, and the size of the mesh has a significant influence on both the time and accuracy of the numerical calculation. The mesh size was analyzed, as shown in Figure 6. The 1 mm mesh is as discerning as the 0.5 mm mesh and decreases the computation time. Therefore, the mesh of the grooved conical tube components was 1 mm in size. The basic physical parameters of the grooved conical tube's materials are shown in Table 2 [25].

Table 2. Basic physical parameters of T700L steel.

Materials	Density (kg/m ³)	Young's Modulus (GPa)	Poisson's Ratio	Yield Strength (MPa)
T700L	7850	203	0.3	730

4.2. Axial Impact Response of the Grooved Conical Tubes

The deformation morphology of different structural types of grooved conical tube components under the axial impact process is collected and organized in Table 3.

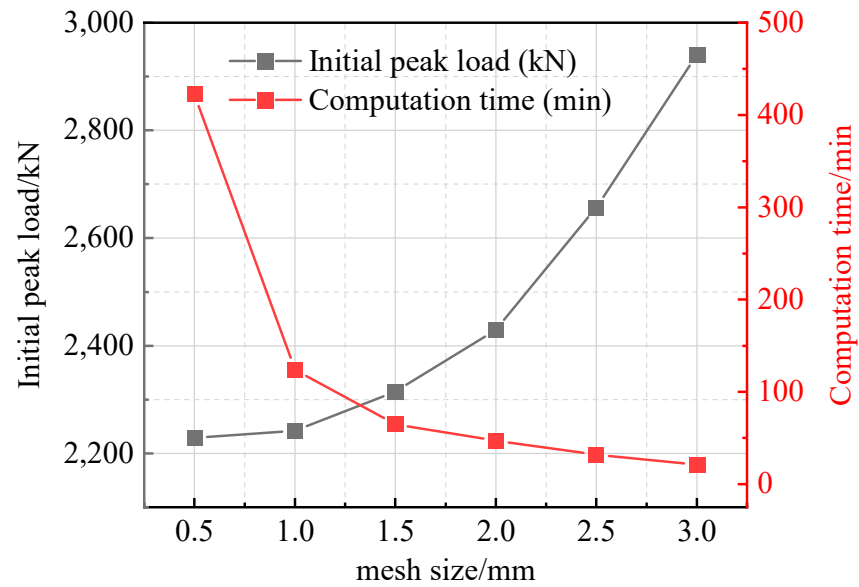
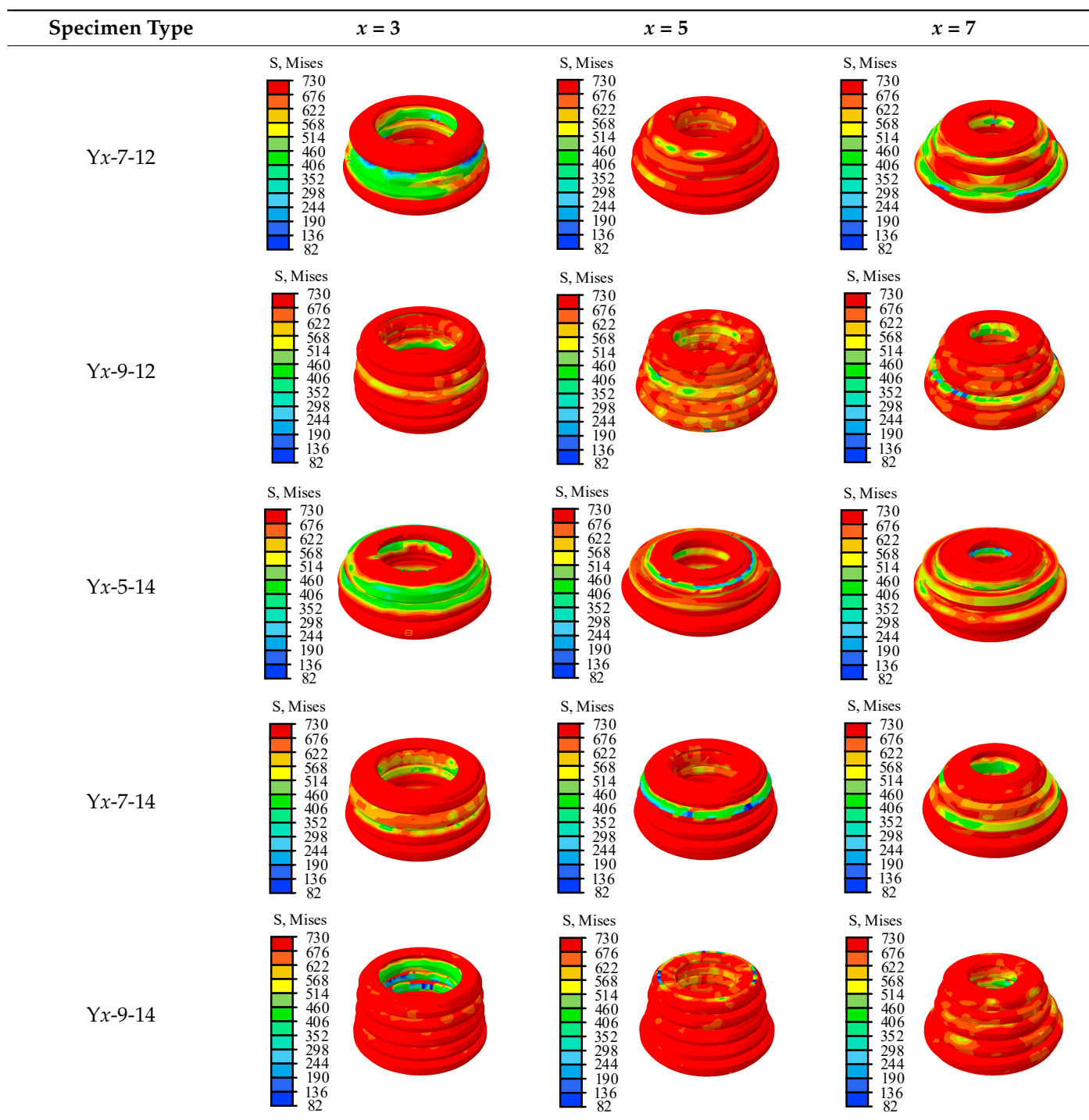


Figure 6. Sensitivity analysis of the mesh.

Table 3. Axial impact deformation of grooved conical tube.

Specimen Type	$x = 3$	$x = 5$	$x = 7$
Yx-5-10			
Yx-7-10			
Yx-9-10			
Yx-5-12			

Table 3. Cont.



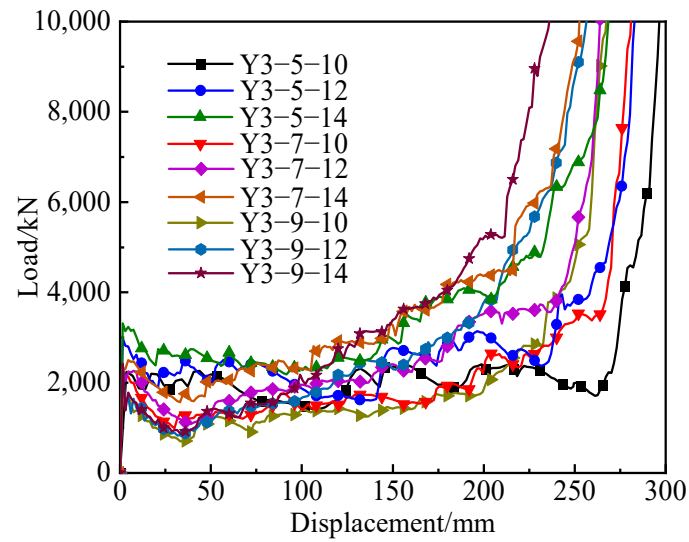
According to Table 3, among the 27 types of simulation results, 24 of the types of grooved conical tubes experienced an accordion deformation mode, and the Y5-5-10, Y7-5-10 and Y7-5-12 conical tubes exhibited a mixed deformation mode. In the grooved conical tube structure, the mixed deformation mode is more likely to occur when the number of cone angles is large, the wall thickness is small and the number of grooves is small. When the height and the bottom radius of the grooved conical tube remain constant, the top radius of the conical tube decreases with an increase in the number of cone angles, which narrows the space inside the conical tube and reduces its effective deformation space. In addition, when the width of the groove equals the wall thickness of the conical tube and

the depth is half the wall thickness of the conical tube, the groove sizes on the inner and outer walls of the conical tube decrease as the wall thickness decreases. The deformation amplitude of the grooved conical tube is reduced, and insufficient plastic hinges form during the buckling deformation process, making a mixed deformation mode more likely under an axial impact.

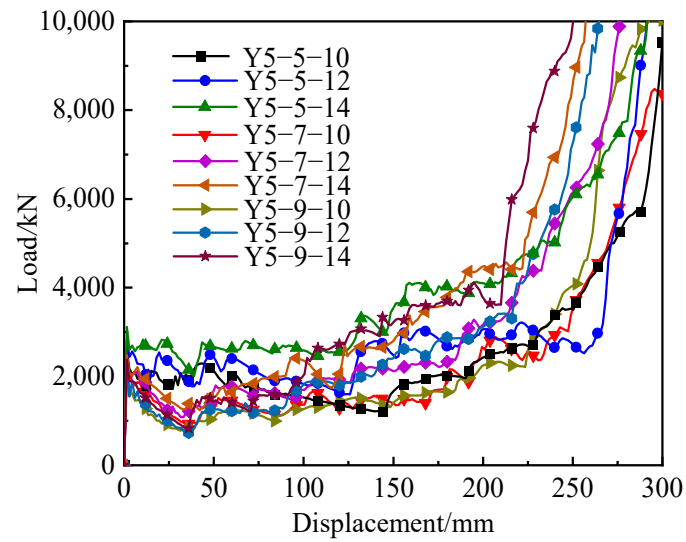
Figure 7 shows the curves of the variation in the load with the displacement of the grooved conical tubes of different structural types. According to Figure 7, the load–displacement curves for the grooved conical tubes during deformation are divided into three phases: (1) the elastic phase, where the grooved conical tube first deforms under the impact load, and the load immediately increases to the P_{max} ; (2) the plastic phase, where the load fluctuates regularly after the P_{max} , and the grooved conical tube begins to undergo large plastic deformation; and (3) the compaction phase, where the grooved conical tube is compressed into a compact state, and the load immediately increases. Based on the load–displacement curves for each type of grooved conical tube during buckling, the performance evaluation parameters for the grooved conical tubes are calculated, as shown in Figure 8.

According to Figure 8, with an increase in the wall thickness, the number of units resistant to deformation during the axial impact increases, resulting in an obvious increase in the initial peak load and effective energy absorption. However, the plastic deformation is not sufficient, and the compaction stage is entered in advance in the buckling process, resulting in the buckling length of the grooved conical tube being reduced and the mean square error increasing. With the increase in the number of grooves, the plastic hinges formed in the buckling process increase. Because the deformation stiffness of the grooved conical tube is lower than that at other positions, its deformation occurs first. The initial peak load of the grooved conical tube decreases, the effective energy absorption decreases and the mean square error increases. As the number of cone angles increases, the top radius of the grooved conical tube decreases, and the inner space of the grooved conical tube shrinks, which leads to a decrease in the effective deformation space inside the grooved conical tube. The initial peak load, effective deformation distance and effective energy absorption tend to decrease due to the decrease in the number of elements that can resist deformation.

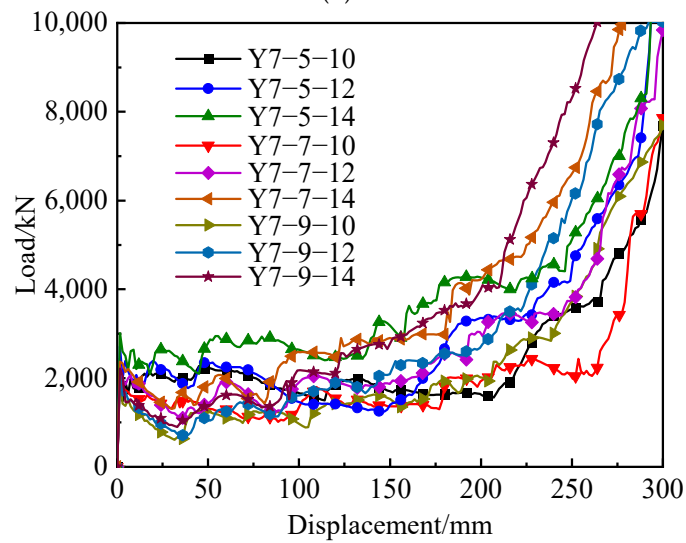
Based on the results on the axial impact of the grooved conical tube, the energy absorption characteristics of the grooved conical tube were analyzed, and the structure of the grooved conical tube energy absorption component conforming to a ZHD6000-type support was selected. (1) As shown in Table 3, the grooved conical tubes that do not conform to the accordion deformation mode are Y5-5-10, Y7-5-10 and Y7-5-12. (2) The rated resistance of a column is 1963 kN, based on Equation (1), $1963 \text{ kN} < P_{max} < 2944.5 \text{ kN}$. Based on the initial peak load of the grooved conical tube shown in Figure 8a, the types of grooved conical tubes that do not meet these requirements are Y3-9-10, Y3-5-12, Y3-5-14, Y5-5-14 and Y7-5-14. (3) As shown in Figure 8e, the Y3-7-12, Y5-7-12, Y7-7-12, Y3-9-12, Y5-9-12, Y7-9-12, Y3-7-7-14, Y5-7-7-14, Y3-9-14, Y5-9-14, Y5-9-14 and Y7-9-14 grooved conical tubes have a higher load mean square error, so they are excluded. (4) As shown in Figure 8c, the Y3-7-10, Y5-7-10, Y7-7-10, Y5-9-10 and Y7-9-10 grooved conical tubes have low effective energy absorption, so they are excluded. (5) For the remaining Y3-5-10 and Y5-5-12 grooved conical tubes, based on the performance evaluation parameters of the grooved conical tubes in Figure 8, the effective energy absorption of Y5-5-12 is greater than that of Y3-5-10. However, the effective deformation distance is smaller, and the mean square error is larger. Considering the deformation mode and the evaluation parameters of the grooved conical tube component, the Y3-5-10-type grooved conical tube is selected as the component for the ZHD6000-type support.



(a)



(b)



(c)

Figure 7. Load–displacement curves for different types of grooved conical tubes. (a) 3. (b) 5. (c) 7.

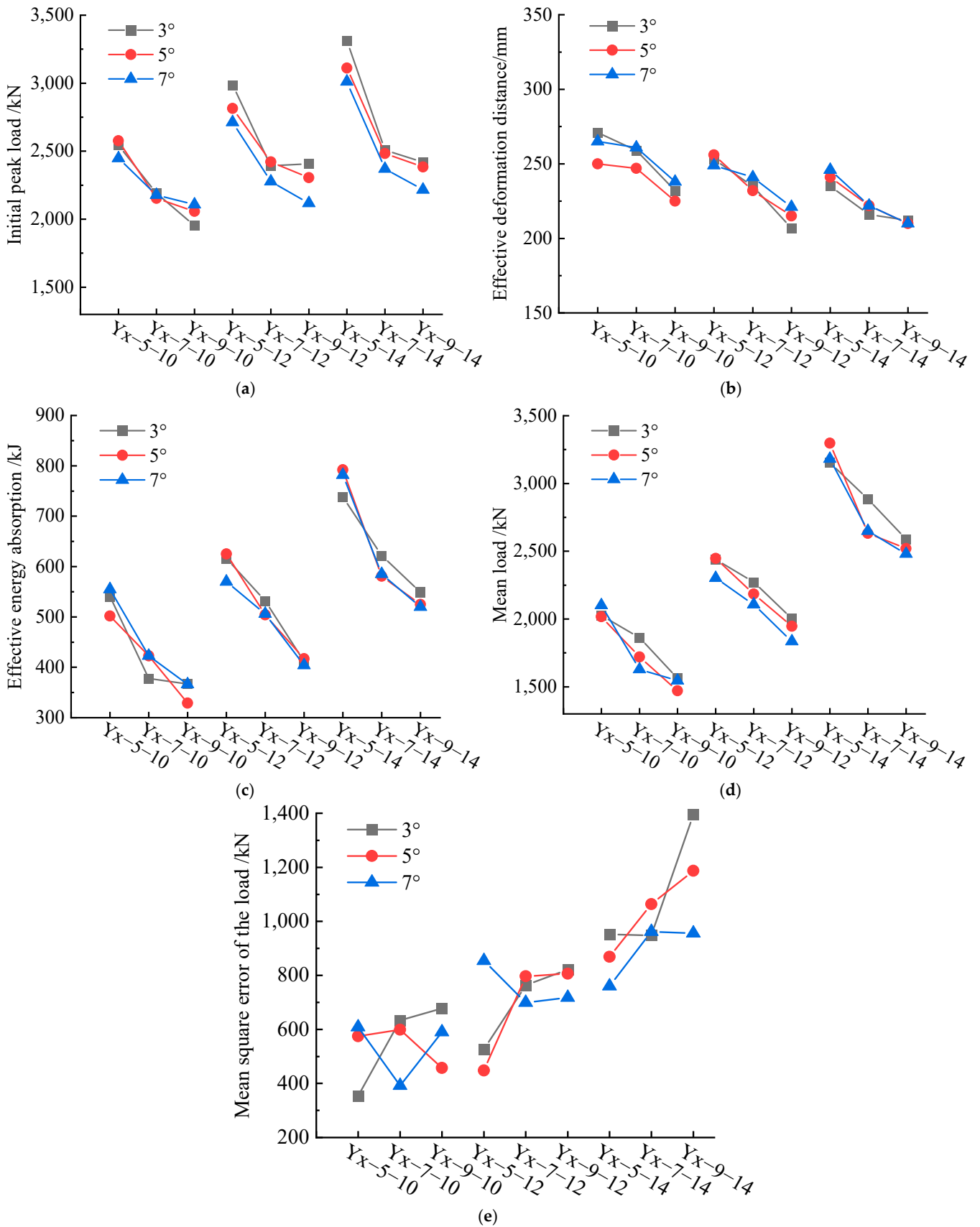


Figure 8. Performance evaluation parameters of grooved conical tubes. (a) Initial peak load. (b) Effective deformation distance. (c) Effective energy absorption. (d) Mean load. (e) Mean square error of the load.

Taking a grooved conical tube with a 3° cone angle as the research object, the structural dimensions of the grooved conical tube are examined in Section 3 to derive the equivalent axial load prediction formula for the grooved conical tube under an axial impact, and the equivalent axial load is obtained. The accuracy of the equivalent axial load theoretical model was verified by comparing the mean load for each type of grooved conical tube with the simulation calculation, as shown in Figure 9. By comparing the equivalent axial load prediction formula with the simulation calculation results, it can be found that the errors in an equivalent axial load of the Y3-5-10, Y3-5-14, 3-7-12, Y3-7-14 and Y3-9-10 types of grooved conical tubes are low, which are 2.42%, 3.01%, 0.70%, 0.14% and 3.07%, respectively. The equivalent axial load error for the Y3-9-14 grooved conical tube is 9.19%. For the Y3-5-12, Y3-7-10 and Y3-9-12 grooved conical tubes, the equivalent axial load errors between the theoretical and simulation results were 7.87%, -5.96% and 7.83%, respectively. These results show that the equivalent axial load prediction formula is accurate and agrees well with the simulation results. The equivalent axial load prediction formula plays a guiding role in the structural design of and material selection for grooved conical tubes.

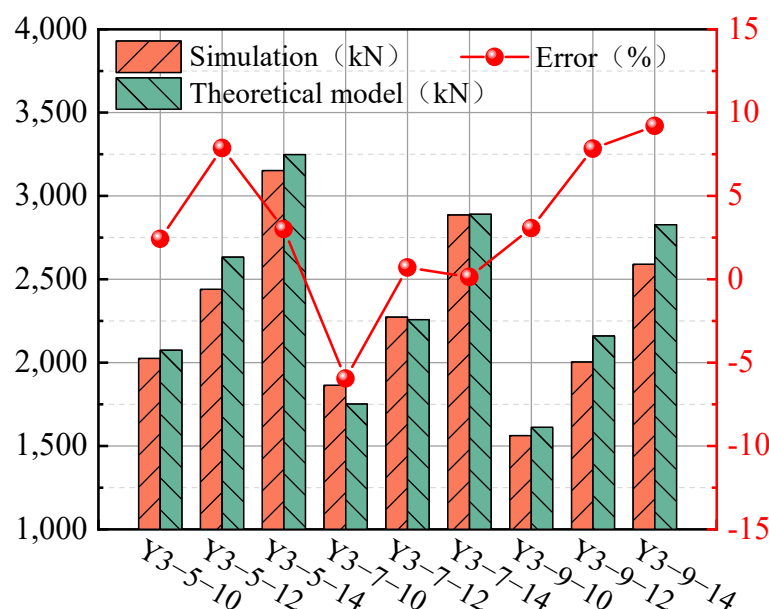


Figure 9. Theoretical and simulation results.

5. Multi-Objective Optimization of Grooved Conical Tubes

5.1. Multi-Objective Optimization Problem Description

Figure 10 shows the load–displacement curve of the Y3-5-10 grooved conical tube. It can be seen from Figure 10 that the part with a large load fluctuation corresponds to the stage when the third groove in the grooved conical tube forms a plastic hinge. In Section 4, a grooved conical tube structure suitable for the ZHD6000 anti-impact support with the optimal cone angle, wall thickness and number of grooves is obtained, and the impact of a change in the groove size on the performance of the grooved conical tube is studied further.

The width and depth of the third groove in the Y3-5-10-type grooved conical tube were selected as the main parameters, and 25 sample points were selected in the design domain of the width and depth of the groove using the full factor experimental design. The multi-objective energy absorption characteristics of the third groove structure were optimized from two perspectives: the load mean square error and effective energy absorption. The groove width varies in the range from 9 mm to 11 mm, and the groove depth varies in the range from 4.8 mm to 5 mm. The remaining parameters, such as the height, wall thickness, cone angle and material properties of the grooved conical tube, are still the same as those

for the Y3-5-10-type grooved conical tube components. The performance of the grooved conical tube with different groove sizes is calculated using simulation, and the full factor test scheme and its energy absorption performance are shown in Table 4.

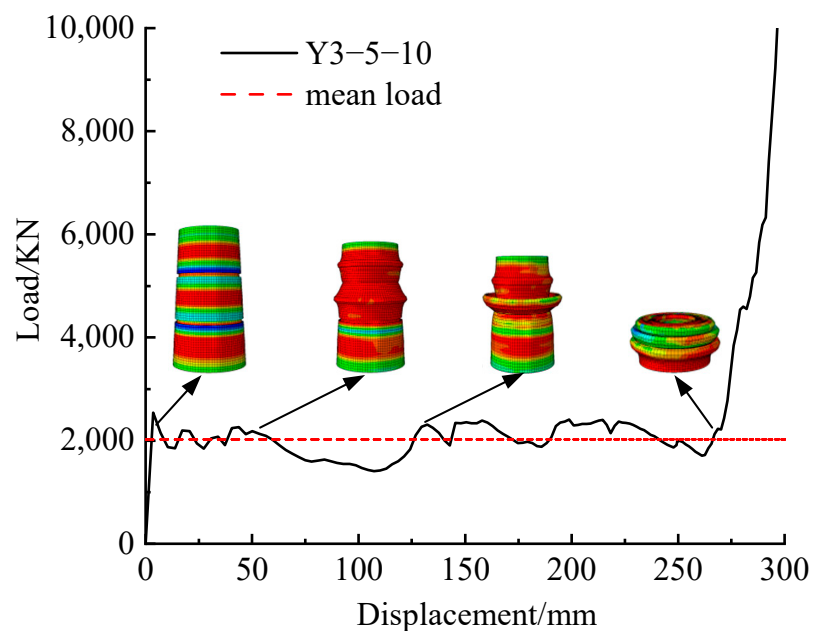


Figure 10. Load–displacement curve of Y3-5-10-type grooved conical tube.

Table 4. Results of the full factor experimental scheme and the energy absorption performance.

Specimen Number	w/mm	d/mm	E_{tot}/kJ	σ/kN
1	9.00	4.80	589.4	318.4
2	9.00	4.85	580.4	330.6
3	9.00	4.90	571.2	343.8
4	9.00	4.95	559.6	357.9
5	9.00	5.00	550.8	373.0
6	9.50	4.80	586.9	305.7
7	9.50	4.85	575.9	317.9
8	9.50	4.90	567.5	331.0
9	9.50	4.95	556.8	345.0
10	9.50	5.00	546.9	360.0
11	10.00	4.80	586.2	300.0
12	10.00	4.85	575.1	312.1
13	10.00	4.90	562.6	325.1
14	10.00	4.95	551.9	339.1
15	10.00	5.00	540.9	354.0
16	10.50	4.80	575.4	301.3
17	10.50	4.85	566.7	313.3
18	10.50	4.90	550.6	326.2
19	10.50	4.95	543.3	340.1
20	10.50	5.00	530.7	354.9
21	11.00	4.80	570.5	301.5
22	11.00	4.85	559.2	315.5
23	11.00	4.90	546.5	329.6
24	11.00	4.95	537.6	343.6
25	11.00	5.00	529.4	357.6

5.2. A Radial Basis Function Model

Commonly used surrogate models include Kriging [26,27], polynomial response surface [28,29], moving least squares [30,31] and radial basis function [32–34] models. By comparing their calculation accuracy, their implementation difficulty and the robustness of these models, the radial basis function model is selected as the surrogate model for the structural optimization of the grooved conical component. The radial basis function surrogate model takes the sample points in the design space as the centers, and the Euclidean distance between the prediction point and the sample points is the independent variable [35]. Different radial basis functions are selected and fitted, and the function values at unknown points are estimated using the fitted functions. The expression of the radial basis function surrogate model is [36]:

$$\hat{f}(x) = \sum_{i=1}^n w_i \varphi(\|x - x_i\|) \quad (16)$$

where $\varphi(\|x - x_i\|)$ is the radial basis function, $\|x - x_i\|$ is the Euclidean distance between the experimental sample point and the predicted point and w_i is the weight coefficient.

The experimental sample points and function values are substituted into Equation (16), and then Equation (16) can be written in matrix form [37] as:

$$Y = \Phi W \quad (17)$$

where $Y = [\hat{f}(x_1), \hat{f}(x_2), \dots, \hat{f}(x_n)]^T$, $\Phi = [\varphi_{ij}] = [\varphi(\|x - x_i\|)](i, j = 1, 2, \dots, n)$.

The actual response value at the experimental sample points used to establish the surrogate model is equal to the approximate value of the surrogate model, and the degree of fit of the surrogate model cannot be verified using the experimental sample points. Therefore, the degree of fit of the surrogate model was verified using the *RMSE* and the R^2 of additional test points (excluding the experimental sample points). The calculation formulas for the *RMSE* and R^2 are as follows [38]:

$$\begin{cases} R^2 = 1 - \frac{\sum_{i=1}^n (f_i - \hat{f}_i)^2}{\sum_{i=1}^n (f_i - \bar{f}_i)^2} \\ RMSE = \sqrt{\frac{\sum_{i=1}^n (f_i - \bar{f}_i)^2}{n}} \end{cases} \quad (18)$$

where n is the number of test points, \hat{f}_i is the radial basis function response value of the additional test points and \bar{f}_i is the simulation result for the additional test points.

In math, the multi-objective optimization problem [36] is expressed as:

$$\begin{cases} \min & f_1(x_1, \dots, x_n) \\ & \dots \\ \min & f_p(x_1, \dots, x_n) \\ \text{s.t.} & g_i(x) \geq 0, \quad i = 1, 2, \dots, m \\ & h_i(x) = 0, \quad i = 1, 2, \dots, l \end{cases} \quad (19)$$

We solve the p single-objective problems in Equation (19):

$$\min_{x \in D} f_j, j = 1, 2, \dots, p \quad (20)$$

Suppose that a single-objective optimization value in a multi-objective optimization problem is f_j^* ; $f^* = (f_1^*, \dots, f_p^*)^T$ is an ideal point in the multi-objective optimization problem. However, the ideal point is usually difficult to reach. Therefore, the nearest point f from the ideal point is found as its optimal value by constructing the evaluation function.

$$\varphi(z) = \sqrt{\sum_{i=1}^p (z_i - f_i^*)^2} \quad (21)$$

We minimize $\varphi[f(x)]$ as:

$$\min_{x \in D} \varphi[f(x)] = \sqrt{\sum_{i=1}^p [f_i(x) - f_i^*]^2} \quad (22)$$

The optimal solution x^* is the optimal solution of Equation (19).

Therefore, the multi-objective optimization problem for grooved conical tubes can be expressed as:

$$\begin{cases} \min & f_1(x) = -E_{\text{tot}}(w, d) \\ \min & f_2(x) = \sigma(w, d) \\ \text{s.t.} & 9 \leq w \leq 11 \\ & 4.8 \leq d \leq 5 \end{cases} \quad (23)$$

5.3. The Ideal Point Method for Multi-Objective Optimization

Based on the full factor test [39], the energy absorption response of the sample points using grooves of different sizes was obtained, and the response functions of the mean square error and the effective energy absorption with respect to the depth and width of the grooves were obtained.

- (1) The fitting result of the load mean square error regression equation:

$$\sigma(w, d) = 3853 - 232.3w - 1224d + 10.686w^2 + 150.3d^2 + 2.36wd \quad (24)$$

- (2) The fitting result of the effective energy absorption regression equation:

$$E_{\text{tot}}(w, d) = 2452 + 89.6w - 720d - 2.566w^2 + 63.2d^2 - 10.12wd \quad (25)$$

The optimal values of the load mean square error and effective energy absorption within the design domain are calculated, as shown in Table 5. The optimal load mean square error is 298.4 kN, and the optimal design variables are $w = 10.34$ mm and $d = 4.80$ mm. The optimal value of effective energy absorption is 613.5 kJ, and the optimal design variables are $w = 9.00$ mm and $d = 4.80$ mm. It can be seen that the optimal solutions for σ and E_{tot} cannot reach their optimal values simultaneously.

Table 5. Optima of single-objective functions for σ and E_{tot} .

Single-Objective Function	w/mm	d/mm	E_{tot}/kJ	σ/kN
Min σ	10.34	4.80	581.2	298.4
Max E_{tot}	9.00	4.80	613.5	317.53

Therefore, it is indispensable to carry out multi-objective optimization for the third groove size for the grooved conical tube. The multi-objective optimization solution is an equilibrium solution of a set of indicators called a Pareto frontier solution set [40]. The Pareto-optimal solution set for the load mean square error and effective energy absorption

is obtained using a genetic algorithm. The global optimal solution is obtained using the ideal point method. The load mean square error and the optimal value in terms of effective energy absorption obtained using the ideal point method are 298.4 kN and 581.2 kJ, respectively. The groove width and depth are 10.34 mm and 4.80 mm, respectively, which have been shown to meet the needs of the ZHD6000 anti-impact support energy absorption components. Figure 11 shows the structure of the grooved conical tube components after multi-objective optimization.

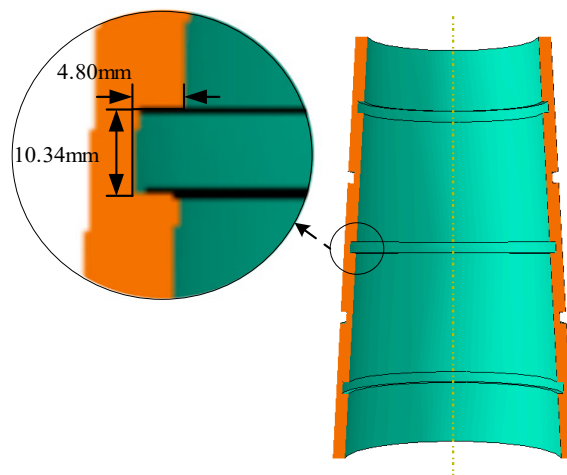


Figure 11. Optimized structure of grooved conical tube component.

According to Table 6, when the width of the third groove is 10.34 mm and the depth is 4.80 mm, the relative error between the simulation results of the Y3-5-10 grooved conical tube components and the regression equation fitting results is small, in which the relative error in the mean square error is 1.67%, and the relative error of the effective energy absorption is 1.38%. The reliability of the radial basis function surrogate model and the ideal point method for solving multi-objective optimization is verified, and it meets the requirements of engineering design.

Table 6. Comparison of multi-objective optimization and simulation results.

Optimization Objective	Optimization Result	Simulation Result	Error/%
σ /kN	298.4	293.5	1.67
E_{tot} /kJ	581.2	573.3	1.38

Figure 12 shows the variation in the load with displacement during the impact process when the performance of the grooved conical tube reaches the optimal value for this multi-objective optimization problem and compares it with that of the Y3-5-10-type grooved conical tube before optimization. According to Figure 12, compared with the Y3-5-10-type grooved conical tube, the load fluctuation in the optimized components is smaller, and the buckling process is more stable without reducing the effective energy absorption of the original components, which achieves the purpose of the optimization.

As shown in Table 6, the mean square error of the grooved conical tube after optimization is 293.5 kN, which is 20.6% lower than the 354.0 kN before optimization. After optimization, the effective energy absorption of the grooved conical tube is 573.3 kJ, which is 6.0% higher than that of 540.9 kJ before optimization. The results show that optimizing the size of the third groove in the grooved conical tube can significantly reduce the load fluctuation in the grooved conical tube during the axial impact process without reducing the effective energy absorption of the original grooved conical tube components, with

the grooved conical tube components effectively playing an energy-absorbing role and improving the structural safety, which provides a reference for the design and optimization of other structural components.

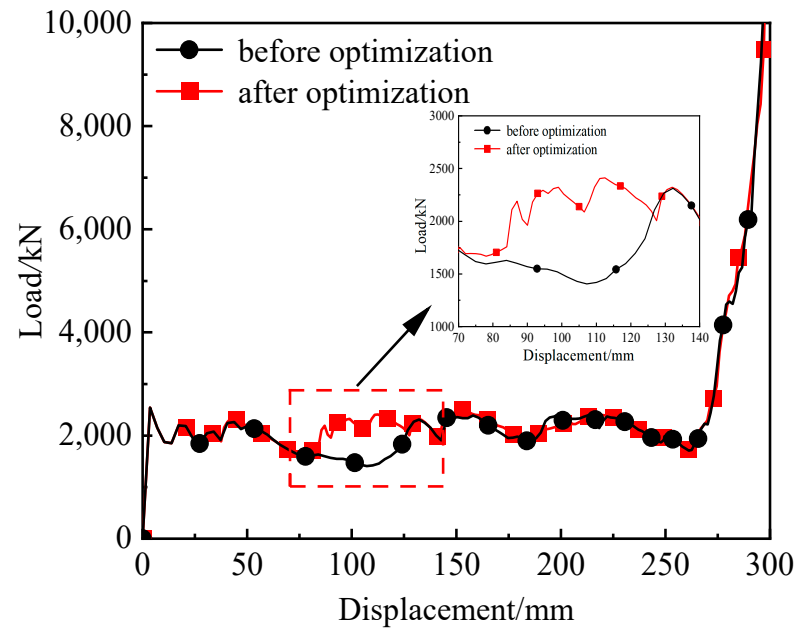


Figure 12. Load–displacement curve of grooved conical tube component.

5.4. Comparison of the Energy Absorption Performance Between a Grooved Conical Tube and a Corrugated Square Tube

The performance of the optimized grooved conical tube and a widely used corrugated square tube is compared and analyzed. Mises stress nephograms of the deformation process for the grooved conical tube and the corrugated tube are shown in Figure 13, and the load–displacement curves are collected and organized in Figure 14.

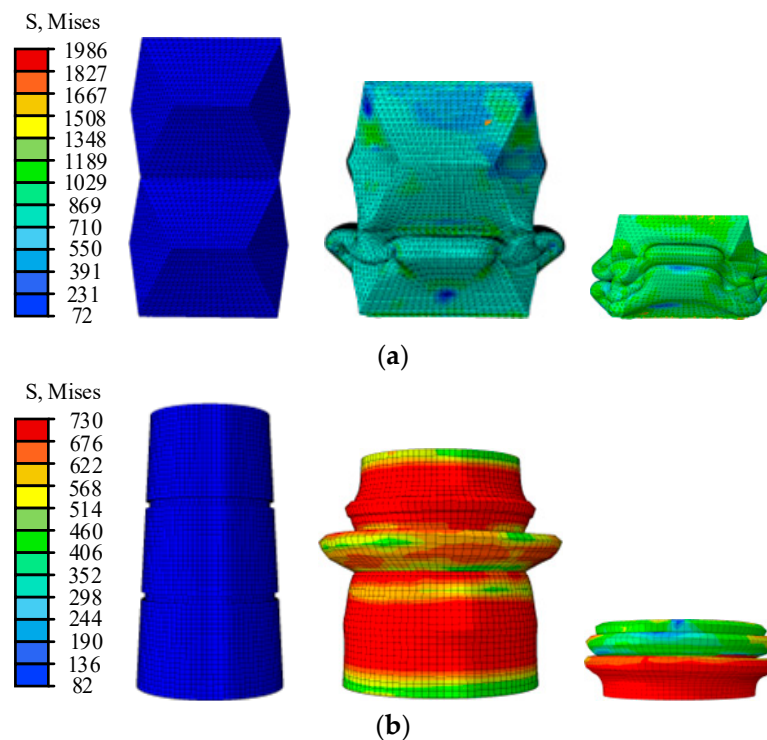


Figure 13. Deformation morphology of grooved conical tube and corrugated square tube. (a) Corrugated square tube. (b) Grooved conical tube.

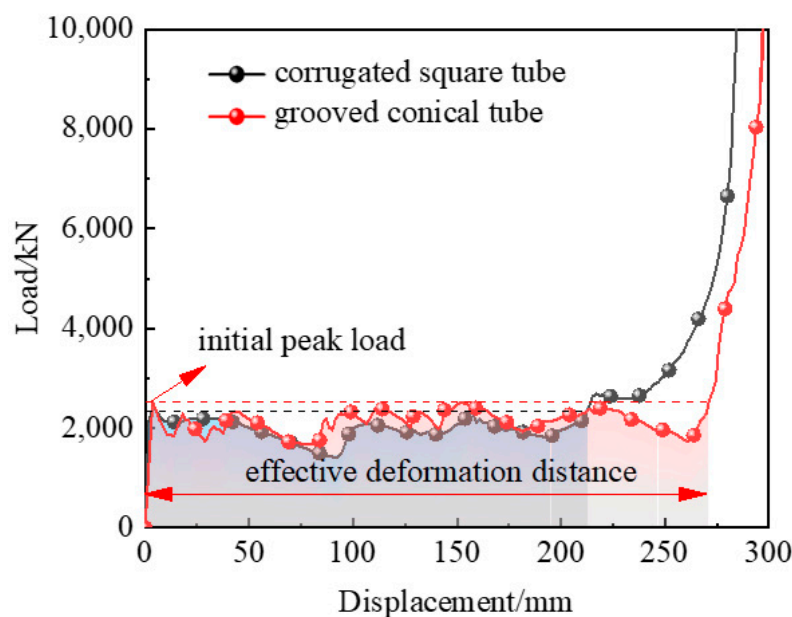


Figure 14. Load–displacement curves of grooved conical tube and corrugated square tube.

As shown in Figure 13, axisymmetric folding deformation occurs in both the grooved conical and corrugated square tubes, and the deformation mode is stable and reliable. As shown in Figure 14, the trend in terms of the variation in the load of the corrugated square tube and the grooved conical tube in the elastic phase is the same; the load quickly reaches the initial peak load, and the load enters a regular state of fluctuation after reaching the initial peak load in the plastic phase. However, the corrugated square tube enters the compaction phase faster than the grooved conical tube. When the buckling length of the corrugated square tube is 213 mm, the load of the corrugated square tube reaches the initial peak load for the second time, while that of the grooved conical tube reaches the initial peak load for the second time when the buckling length is 271 mm. It can be seen that the grooved conical tube has more advantages than the corrugated square tube in its effective deformation distance and effective energy absorption.

According to Table 7, the performance of the grooved conical tube and the corrugated tube shows that the initial peak load, mean load and load mean square error of the grooved conical tube are the same as those of the corrugated tube, the effective deformation distance of the grooved conical tube is increased by 27.2% and the effective energy absorption is increased by 37.1%. Compared with the corrugated square tube, the effective deformation distance of the grooved conical tube increases, and more energy can be absorbed under the same mean load condition. The grooved conical tube has relative advantages in terms of its effective deformation distance and effective energy absorption. It provides sufficient time to open the relief valve of the hydraulic support column, which is crucial for the prevention of rockbursts.

Table 7. Energy absorption performance of grooved conical tube and corrugated square tube.

Component	P_{max}/kN	δ_{ef}/mm	E_{tot}/kJ	P_{mean}/kN	σ/kN
corrugated square tube	2374	213	418	1969	213
grooved conical tube	2543	271	573	2026	293

6. Conclusions

Rockbursts are a serious hazard in engineering. The grooved conical tube component can enhance the performance of the support and effectively prevent and control rockbursts.

In this study, the effects of the cone angle, number of grooves and wall thickness on the performance of a groove conical tube are considered, and the groove width and depth of the groove conical tube components are optimized. Based on the results, the following conclusions are drawn:

1. Based on a theoretical model of the axisymmetric plastic collapse of a thin-walled circular tube, the energy dissipation path of the grooved conical tube component is analyzed, and an equivalent axial load theoretical model for the grooved conical tube component under an axial impact is established. The results of the equivalent axial load theoretical model agree well with those of the simulations.
2. A grooved conical tube energy absorption component is proposed for use in anti-impact support columns. The deformation of the energy absorption components tends to be more stable in an accordion deformation mode. The performance of different structural types of grooved conical tube components is analyzed, and the Y3-5-10-type grooved conical tube components have a noticeably greater energy absorption performance as the energy absorption components of the anti-impact support.
3. Without reducing the performance of the Y3-5-10-type grooved conical tube component, the mean square error of this component is reduced by 20.6% using multi-objective optimization, and the effective energy absorption is increased by 6.0%. Compared with the original energy absorption component, the optimized grooved conical tube component has a more stable and safe energy absorption performance.
4. Compared with the widely used corrugated square tube, the effective deformation distance of the grooved conical tube is increased by 27.2%, and the effective energy absorption is increased by 37.1%. The grooved conical tube provides sufficient time to open the relief valve of the hydraulic support column, which is crucial for the prevention of rockbursts. Future studies should verify these findings further, fabricate the optimized grooved conical tube components as physical objects and verify their energy absorption properties through axial impact tests.

Author Contributions: Conceptualization, Z.L.; Methodology, J.X.; Software, Z.L.; Validation, Z.L. and J.X.; Formal analysis, Z.L.; Resources, X.X.; Data curation, X.X.; Writing—original draft, J.X.; Writing—review & editing, B.S.; Supervision, B.S. All authors have read and agreed to the published version of the manuscript.

Funding: The research was funded by the National Natural Science Foundation of China (Nos. 52204092 and 52274203).

Data Availability Statement: The original contributions presented in this study are included in the article. Further inquiries can be directed to the corresponding authors.

Conflicts of Interest: The authors declare no conflicts of interest.

References

1. Li, X.; Li, L.; Yan, Y.; Qi, C. A micro-macro fracture model for evaluating the brittle-ductile transition and rockburst of rock in true triaxial compression. *Int. J. Rock. Mec. Min. Sci.* **2025**, *186*, 105993. [[CrossRef](#)]
2. Dai, J.; Gong, F.; Huang, D.; Zhang, Q. Quantitative evaluation method of rockburst prevention effect for anchoring rock masses around deep-buried tunnels. *Tunn. Undergr. Space Technol.* **2025**, *156*, 106268. [[CrossRef](#)]
3. Cheng, S.; Yin, X.; Gao, F.; Pan, Y. Microseismic Data-Driven Short-Term Rockburst Evaluation in Underground Engineering with Strategic Data Augmentation and Extremely Randomized Forest. *Mathematics* **2024**, *12*, 3502. [[CrossRef](#)]
4. Wu, W.; Gong, F.; Zhang, Z. Sidewall rockburst characteristics of highly stressed circular tunnel under impact load. *J. Rock. Mec. Geo Eng.* **2024**, *16*, 4909–4924. [[CrossRef](#)]
5. Shen, Y.; Wu, S.; Wang, Y.; Wang, J.; Yang, Z. Interpretable model for rockburst intensity prediction based on Shapley values-based Optuna-random forest. *Underground Space* **2025**, *21*, 198–214. [[CrossRef](#)]

6. Wang, Y.; Ma, G.; Rezanian, M. A granular anisotropic model of underground rockburst considering the effect of radial stresses. *Tunn. Undergr. Space Technol.* **2025**, *155 Pt 1*, 106202. [[CrossRef](#)]
7. Pan, Y.S.; Qi, Q.X.; Wang, A.W.; Xiao, Y.H.; Chen, Y.X.; Lv, X.F.; Xu, L.M.; Dai, L.P. Theory and technology of three levels support in bump-prone roadway. *J. China Coal Soc.* **2020**, *45*, 1585–1594.
8. Pan, Y.S.; Xiao, Y.H.; Li, Z.H.; Wang, K.X. Study of tunnel support theory of rockburst in coal mine and its application. *J. China Coal Soc.* **2014**, *39*, 222–228.
9. Ma, X.; Pan, Y.S.; Xiao, Y.H. Study on Application of the Mine Anti-Impact and Energy-Absorption Device. *Appl. Mech. Mater.* **2013**, *470*, 598–603. [[CrossRef](#)]
10. Ma, X.; Pan, Y.S.; Zang, J.Z.; Xiao, Y.H. Design and energy-absorbing performance of core energy-absorbing components of anti-shock support. *J. China Coal Soc.* **2018**, *43*, 1171–1178.
11. Tian, L.Y.; Zhou, Y.P.; Sun, Y.X.; Yu, N. Energy absorption performance of multicellular thin-walled energy-absorbing components of anti-shock support columns. *J. China Coal Soc.* **2023**, *48*, 2224–2235.
12. Tian, L.; Yu, X.; Zhou, Y.; Sun, Y.; Yu, N. Optimization simulation and crushing experiment of anti-impact energy absorption component of hydraulic support column. *J. China Coal Soc.* **2024**, *49*, 2924–2936.
13. Hao, Z.Y.; Liu, Y.Q.; Pan, Y.S. Experimental study on filling material of mining buffer energy absorption device. *J. Min. Saf. Eng.* **2018**, *35*, 620–628.
14. Yang, J.W.; Tang, Z.; He, F.; Zhang, Y.Y.; Yu, Y.J. Energy absorption and anti-impact properties of mine diameter-expanding energy absorption components. *J. Vib. Shock.* **2015**, *34*, 134–142.
15. Guo, C.; Han, J. Research on energy absorbing components of ZQL hydraulic support. *J. Bra Soc. Mech. Sci. Eng.* **2023**, *45*, 176. [[CrossRef](#)]
16. Wang, C.H.; An, D.; Han, C.; Tang, Z. Simulation and tests for new tubular type energy-absorbing and anti-impact members with stiffened plate under rock burst. *J. Vib. Shock.* **2019**, *38*, 203–210+241.
17. Zhang, J.; Guo, H.; Xiao, Y.; Pan, Y.; Jiang, B.; Su, S.; Ni, B. Design of torsion plate energy-absorbing member and analysis of energy-absorbing and anti-impact characteristics. *Shock. Vib.* **2023**, *2023*, 8966724. [[CrossRef](#)]
18. Wang, C.H.; Niu, H.C.; An, D.; Jiang, H. Research on variable gradient thin-walled energy absorbing component of scour-proof hydraulic support. *Sci. Technol. Eng.* **2020**, *20*, 3546–3551.
19. Qi, Y.; Chi, H.; Liu, X.; Xin, R.; Liu, R.; Yu, S.; Zhang, C.; Mao, C.; Yu, Z.; Xu, Z.; et al. Bionic beetle nickel-titanium medical skeleton with excellent deformation recovery ability and mechanical properties. *Thin-Walled Struct.* **2025**, *208*, 112817. [[CrossRef](#)]
20. Alexander, J.M. An approximate analysis of the collapse of thin cylindrical shells under axial loadin. *Q. J. Mech. Appl. Math.* **1960**, *13*, 10–15. [[CrossRef](#)]
21. Okutan, S.M.; Genel, K. Effect of inner reinforcement on the torsional load-bearing performance of holed aluminum/composite thin-walled tubes. *Thin-Walled Struct.* **2025**, *208*, 112805. [[CrossRef](#)]
22. Feli, S.; Makhsousse, E.; Jafari, S.S. Dynamic progressive buckling of thin-wall grooved conical tubes under impact loading. *Int. J. Crash* **2020**, *25*, 220–229. [[CrossRef](#)]
23. Miao, X.; Tang, Y.; Li, Q.; Wang, G.; Liu, J.; Wang, F.; Zhang, J. Design of novel sandwich double-hat beams filled with aluminum hierarchical structures under axial impact loading. *Structures* **2024**, *70*, 107758. [[CrossRef](#)]
24. Liu, Y.; Cao, A.; Li, G.; Yang, X.; Wang, C.; Yu, L.; Ju, M. Ground motion characteristics induced by high-magnitude events with different source mechanisms of longwall mining. *Geomat. Nat. Hazards Risk* **2024**, *15*, 2424425. [[CrossRef](#)]
25. Xiao, X.C.; Zhu, H.; Xu, J.; Fan, Y.; Li, Z.; Lei, Y. Research on energy-absorption characteristics of energy-absorption and anti-impact components under axial impact and deflection load. *J. Safety Sci. Technol.* **2023**, *19*, 93–100.
26. Zhang, W.; Guan, Y.; Wang, Z.; Xu, H. A novel active learning Kriging based on improved Metropolis-Hastings and importance sampling for small failure probabilities. *Comp. Meth Appl. Mech. Eng.* **2025**, *435*, 117658. [[CrossRef](#)]
27. Liu, S.; Bai, L.; Zhang, K.; Tan, X.; Zhang, X. Analysing spatial distribution and variability of vadose zone moisture in different subsidence areas using 3D empirical Bayesian kriging and pixel-by-pixel methods. *Earth Sci. Inform.* **2024**, *18*, 44. [[CrossRef](#)]
28. Tamilarasan, A.; Radhika, K.; Rajamani, D.; Renugambal, A. D-optimal-based parametric study for improving the FFFed product quality of the ABS material. *J. Mec. Sci. Tec.* **2024**, *38*, 6225–6235. [[CrossRef](#)]
29. Mu, R.; Zhang, J.; Zhang, L.; He, S. Can government green discourse-behavior congruence mitigate carbon emissions? A polynomial regression with response surface analysis. *Appl. Energy* **2025**, *380*, 125008. [[CrossRef](#)]
30. Nguyen, M.-N.; Hoang, V.-N.; Lee, D. Multiscale topology optimization with stress, buckling and dynamic constraints using adaptive geometric components. *Thin-Walled Struct.* **2023**, *183*, 110405. [[CrossRef](#)]
31. Zhou, M.; Gao, L.; Xiao, M.; Liu, X.; Huang, M. Multiscale topology optimization of cellular structures using Nitsche-type isogeometric analysis. *Int. J. Mec. Sci.* **2023**, *256*, 108487. [[CrossRef](#)]
32. Hao, Z.; Cai, Z.; Zhang, Z. Fractional-order dependent Radial basis functions meshless methods for the integral fractional Laplacian. *Comp. Math. Appl.* **2025**, *178*, 197–213. [[CrossRef](#)]

33. Li, H.; Ni, H.; Fu, J.; Wan, B.; Chu, D.; Fang, F.; Wang, R.; Ma, G.; Zhou, X. A domain-decomposition-based parallel approach for 3D geological modeling using radial basis functions interpolation on GPUs. *Earth Sci. Inform.* **2024**, *18*, 37. [[CrossRef](#)]
34. Jiang, Q.; Zhao, S. A Bessel-Class Radial Basis Function for Neural Networks in Solving Helmholtz and Laplace Equations. *Acta Mech. Solida Sin.* **2024**, preprint. [[CrossRef](#)]
35. Xing, R.; Zhao, Z.; He, C.; Xu, P.; Zhu, D.; Li, Y.; Li, Y.; Yang, Z. Optimizing FBG sensor layout of tunnel monitoring using improved multi-objective snow ablation optimizer based on radial basis function. *Measurement* **2025**, *242*, 116289. [[CrossRef](#)]
36. Vishwanatha, J.S.; Srinivasa Pai, P.; D’Mello, G.; Sampath Kumar, L.; Bairy, R.; Nagaral, M.; Channa Keshava Naik, N.; Lamani, V.T.; Chandrashekar, A.; Yunus Khan, T.M.; et al. Image-processing-based model for surface roughness evaluation in titanium based alloys using dual tree complex wavelet transform and radial basis function neural networks. *Sci. Rep.* **2024**, *14*, 28261. [[CrossRef](#)]
37. Yang, D.; Yang, X.; Chen, Q.; Gong, W.; Zhong, J. Study on microcosmic properties and temperature simulation of foamed polypropylene composites. *Sci. Rep.* **2024**, *14*, 27626. [[CrossRef](#)]
38. Xu, K.; Meng, B.; Wang, Z. Radial basis function neural network based data-driven iterative learning consensus tracking for unknown multi-agent systems. *Appl. Soft Comp.* **2024**, *167*, 112425. [[CrossRef](#)]
39. Yang, N.; Li, Z.; Zhang, L.; Li, L.; Liu, S.; Chen, X.; Wang, H.; Fan, S.; Fan, S.; Xu, J. Full active counter-roller spinning for thin-walled cylinders: Macroscopic deformation mechanism, mesoscopic texture evolution, and forming performance strengthening. *Thin-Walled Struc.* **2025**, *206*, 112634. [[CrossRef](#)]
40. Dunke, F.; Nickel, S. Approximate and exact approaches to energy-aware job shop scheduling with dynamic energy tariffs and power purchase agreements. *Appl. Energy* **2025**, *380*, 125065. [[CrossRef](#)]

Disclaimer/Publisher’s Note: The statements, opinions and data contained in all publications are solely those of the individual author(s) and contributor(s) and not of MDPI and/or the editor(s). MDPI and/or the editor(s) disclaim responsibility for any injury to people or property resulting from any ideas, methods, instructions or products referred to in the content.